Iron related precipitates in multicrystalline silicon by Conductive Atomic Force Microscopy

Pierpaolo Vecchi[a,*], Giovanni Armaroli[a], Marisa Di Sabatino[b], and Daniela Cavalcoli[a]

[a)] *Department of Physics and Astronomy, University of Bologna, Viale Berti Pichat 6/2, 40127 Bologna, Italy*

[b)] *Department of Materials Science and Engineering, NTNU, A. Getz vei 2B, NO-7491 Trondheim, Norway*

[*]Corresponding author. Email address: pierpaolo.vecchi2@unibo.it (P. Vecchi)

Abstract

Multicrystalline silicon (mc-Si) is a widely used material for photovoltaic applications. The presence of metallic contaminated grain boundaries strongly affects the crystal electronic properties enhancing electron-hole recombination, thus reducing the solar cell performance. The present study aims to investigate the electrical activity of metallic contaminated grain boundaries in mc-Si. Two sets of mc-Si wafers, contaminated with iron and aluminium, respectively, were analysed. The wafers presented grain boundaries whose density and character were characterized by Electron Backscatter Diffraction (EBSD), while their electrical activity was analysed using Conductive Atomic Force Microscopy (c-AFM). The grain boundary density decreases along the ingot height and the most common coherent grain boundaries have the character $\Sigma 3^n$. The grain boundary electrical activity is mostly due to metallic precipitates located at the grain boundaries. In particular, iron precipitates enhance the current contrast at the grain boundaries. Both fixed voltage maps and current-voltage characteristics at the grain boundaries were measured to understand and clarify the transport phenomena at grain boundaries decorated with metallic impurities. The current profiles measured by c-AFM across a grain boundary were modelled by assuming the contribution of a Coulombic potential introduced by the positively charged precipitate. Quantitative parameters regarding the segregated iron-related precipitates are estimated from the model. The results of this study, based on local electrical characterization and appropriate modelling, will contribute to improving the understanding of the recombination at iron precipitates at grain boundaries in mc-Si.

Keywords

Silicon, photovoltaics, AFM, impurities

1. Introduction

Multicrystalline silicon (mc-Si) is, together with monocrystalline silicon, the most widely used material in the photovoltaic industry. However, it contains a high density of extended defects, i.e., grain boundaries (GBs) and dislocations, and a wide range of impurities, affecting the output solar cell performance.

GBs and dislocations can be active recombination centres affecting minority carrier lifetime [1] and the recombination activity depends on the character and coherency degree of the boundary [2]. Metal decoration is another factor that enhances the electrical activity, as single impurity atoms introduce deep levels in the bandgap [3]. The nucleation and coarsening of bigger metallic precipitates at the GB introduce metal-like density of states, this forms an internal metal-semiconductor junction with a space charge region that affects the capture rate and the recombination of carriers.

Unintentional contamination by metallic impurities has a detrimental effect on the electrical properties of microelectronic and photovoltaic devices. One of the most common impurities is iron, which is often present in feedstocks [4] and crucibles [5]. Iron limits the bulk minority carrier lifetime of most as-grown *p*-type silicon wafers [6] because of its large electron cross section [7] and the conversion efficiencies typically decrease already at concentrations of few parts per billion [8,9]. The formation and distribution of iron precipitates in silicon ingots [10], the effect of iron contamination in silicon solar cells [11], and defect-engineering techniques to remove such impurities [12,13] have been widely studied in literature.

Iron reaches its solubility limit at high temperatures, but supersaturation is not maintained during the cooling and rapid interstitial diffusion occurs: atoms can either be attracted to dislocations, act as nucleation sites and give rise to decorated dislocations [14], or aggregate and form intermetallic compounds with silicon. Iron disilicides are the most common among those compounds, and $FeSi_2$ exists in two stable forms: α-$FeSi_2$, metastable at room temperature, that decomposes very slowly to β-$FeSi_2$ with a transition temperature of 982°C [15]. Cubic γ-$FeSi_2$ has also been reported as a metastable phase that transforms into β-$FeSi_2$ beyond a certain size [16].

Although iron silicides are known to be detrimental in photovoltaic devices, they can behave as beneficial compounds, as the formation of isolated precipitates of single-crystal β-$FeSi_2$ by ion implantation was used to fabricate a stable working silicon-based LED. Thus, this phase is a potential candidate for an optically active material compatible with the existing silicon technology [17]. This shows that Fe related precipitates in silicon cannot be described just as lifetime-killers, but they have a more complex effect on the optical and electronic properties of silicon.

The electrical activity of decorated GBs in mc-Si is usually investigated with the electron beam induced current (EBIC) technique [3], while conductive atomic force microscopy (c-AFM)

analyses of GBs in silicon are still in their infancy. However, c-AFM is an interesting method in this respect, as it allows to study conductivity with a submicron resolution, which is ideal to observe electrically active precipitates. This technique has already been used on hydrogenated microcrystalline silicon grown by chemical vapor deposition [18–20], but also for the characterization of iron contaminated directionally solidified (DS) mc-Si wafers, which found a higher conductivity at the grain boundaries [21].

In this manuscript structural properties of DS mc-Si wafers are characterized by Electron Backscatter Diffraction (EBSD). Fe and Al contaminated mc-Si wafers are investigated by c-AFM, to study the different electrical behaviour of metallic contaminants at GBs. Current profiles across contaminated GBs are modelled to extract quantitative parameters such as precipitate charge and radius.

2. Materials and methods

The samples investigated in this study were obtained from two DS mc-Si ingots of size G5, grown in a quartz crucible, with a silicon nitride coating. To study the effect of different metallic precipitates on the GBs, one ingot was grown from silicon melt intentionally contaminated with 1000 ppb of iron and the other with 1000 ppb of aluminium. These two metals are the only contaminants that were added intentionally, together with boron as doping species to achieve the targeted electrical resistivity.

Five samples from each ingot were characterized with EBSD, to quantify the density of different types of GBs at different ingot heights. The EBSD measurements were performed using a JEOL JSM 840A Scanning Electron Microscope, equipped with a TSL MSC-2200 unit for beam control, TSL OIM software for data acquisition and analysis, and a NORDIF Phosphor detector at an accelerating voltage of 20.0 kV, tilt angle of 62.5° and a working distance of 30 mm. The samples have an area of 3×3 cm^2 and their surface was polished using sandpaper with a grit size of 9, 3, and 1 micrometers. An area of approximately 23×14 mm^2 was analyzed in each sample. Since the area to be analysed was large, the Comboscan technique was used. With this method, the area of interest was divided in smaller regions, that are scanned sequentially by automatically moving the sample stage, stored and stitched back together. The stage movement is time consuming, thus a low magnification of 27× and a beam step size of 50 μm were used to have more efficient measurements.

Topography and current maps on GBs were obtained by c-AFM. These measurements were carried out with a Park NX10 AFM, placed on an active vibration isolation table, and controlled by a PC with the NX10 Software. During measurements, the room humidity ranged from 35% to 40%. The AFM tip was a Rocky Mountain 25Pt300B, a platinum tip with spring constant 18 N/m and radius below 20 nm. The sample was fixed onto a magnetic sample holder with bi-adhesive tape and

the electrical contact was made with silver paste. All the scans were captured at a rate of 0.30 Hz, with Z-feedback setpoint 449.055 nN, and gain 0.500. The sample is biased at -10.0V and the amplifier gain is 10^9. As wearing or degradation of the Pt coating of the tip might introduce artifacts in the measurements [22], the c-AFM maps were repeated to check for reproducibility. These effects induced by degradation were not observed in the scans. Local current-voltage measurements were acquired on the silicon grains and on the GBs. Results from the characterization of two samples are reported, referred as "Fe contaminated" and "Al contaminated", respectively. Both samples were chosen from the bottom of the ingots, at a height fraction of ≈0.06. Here it is expected a higher density of GBs, that are known to be preferential sites for the segregation of these metallic impurities.

3. Results and discussion

3.1. Microstructural characterization by Electron Backscatter Diffraction

The EBSD map of the Fe contaminated sample is shown as an example in Fig. 1. A representation of the grains can be obtained from orientation image maps, where all individual grains are given a colour depending on their orientation (Fig. 1a).

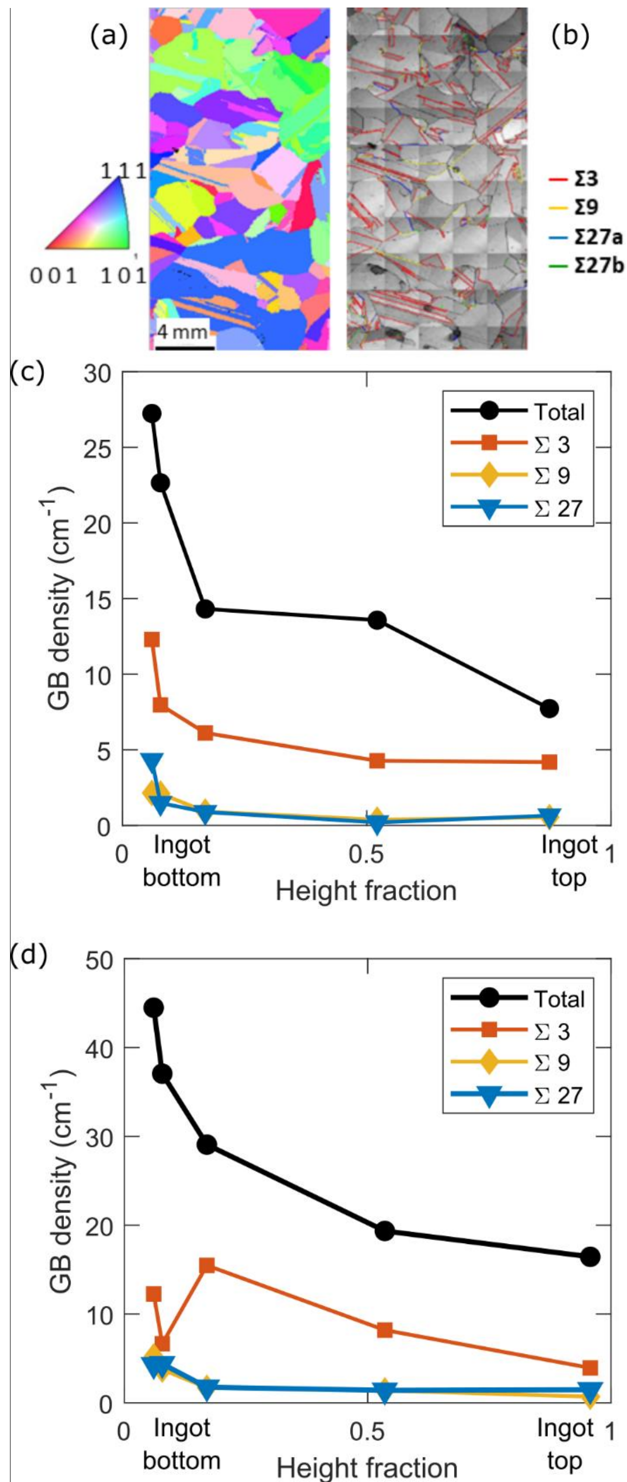

Fig. 1 (a) Inverse pole figure of the Fe contaminated sample showing the grain orientation. (b) EBSD map of the Fe contaminated sample showing the GB character. GB density along the ingot height in the (c) Fe contaminated and (d) Al contaminated ingots.

Fig. 1b shows the coherent GBs with character $\Sigma 3^n$ in the Fe contaminated sample. Fig. 1(c and d) shows how the total GB density and the density of the $\Sigma 3^n$ GB, calculated as the length of the GBs

normalized by the considered wafer area, vary along the height of the iron and aluminium contaminated ingots, respectively. In both ingots the total GB density decreases as a function of height fraction and it is almost halved from the bottom to the middle of the ingot, while from the middle to the top the density becomes more stable, with no noticeable differences [23]. The $\Sigma3^n$ boundaries are the most common coherent boundary in mc-Si [24] and their density also decreases along the ingot height. Other coherent boundaries with a non $\Sigma3^n$ character, such as $\Sigma5$ and $\Sigma11$, exist in a very small density compared to the $\Sigma3^n$ [23].

Adamczyk *et al.* [25] found that recombination active GBs are mostly small-angle GBs (boundaries with misorientation angle below 15°), which were not detected with this setup. Segments of GBs that lack coherence are also recombination active and this is thought to be due to the increased nucleation site density for metallic precipitates. Among the coherent GBs, $\Sigma3$ boundaries are typically inactive, and their recombination activity might be related to the presence of metals, while $\Sigma27$ boundaries have a higher recombination activity especially in the middle and top of the ingot [25]. In fact, $\Sigma27$ are known to be the source of dislocations, but at the bottom of the ingot the density of large dislocation clusters is much smaller, so the effect of these GBs on the electrical properties is reduced [23,26].

3.2. Grain Boundaries characterization by Conductive Atomic Force Microscopy

Fig. 2(a and b) show current AFM maps of the Fe contaminated and Al contaminated sample, respectively. The current maps present a constant background current and dark straight lines, which means high negative current, that are related to recombination active GBs. The topography maps (shown in Figure A1 in the Supplementary Material) do not have any feature that could be responsible for the enhanced current flow. The bottom half of the current map in Fig. 2b shows a higher noise compared to the top half, which was attributed to charge accumulation due to the high applied voltage.

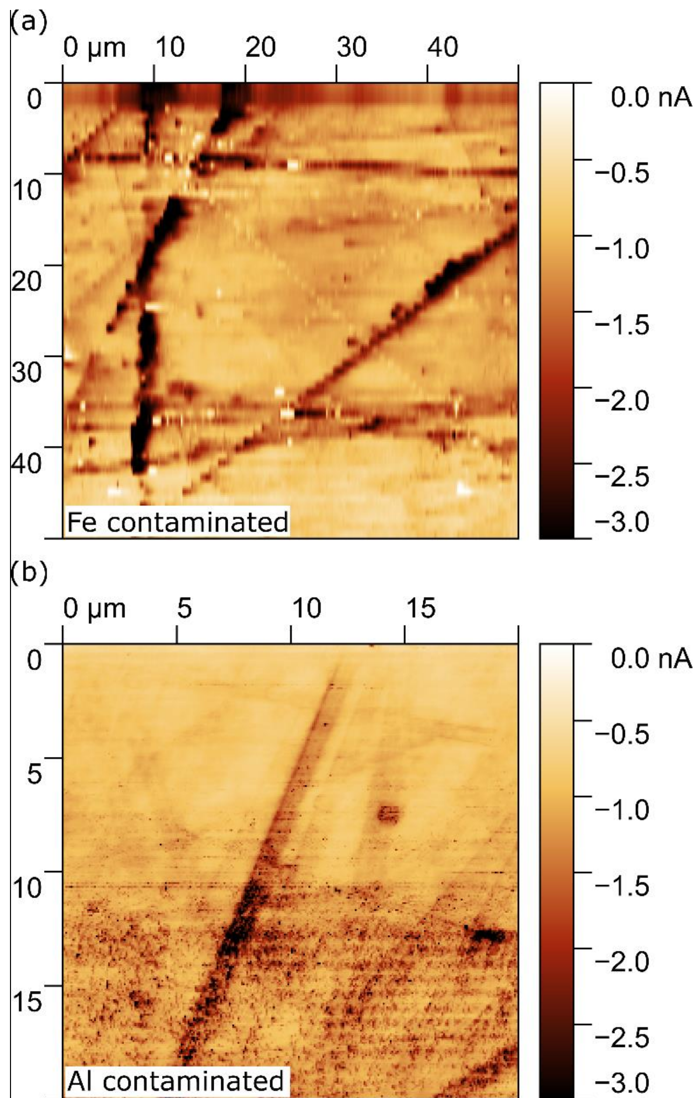

Fig. 2 Conductive Atomic Force Microscopy current maps of the (a) Fe contaminated and (b) Al contaminated samples. Dark regions in the current maps are related to the presence of GBs.

Fig. 3 shows a few current profiles extracted across the GBs in the two samples. The current maximum variation, calculated as the difference between the average value in the grain and the minimum value reached at the boundary, is around -2 nA in the Fe contaminated and around -0.7 nA in the Al contaminated.

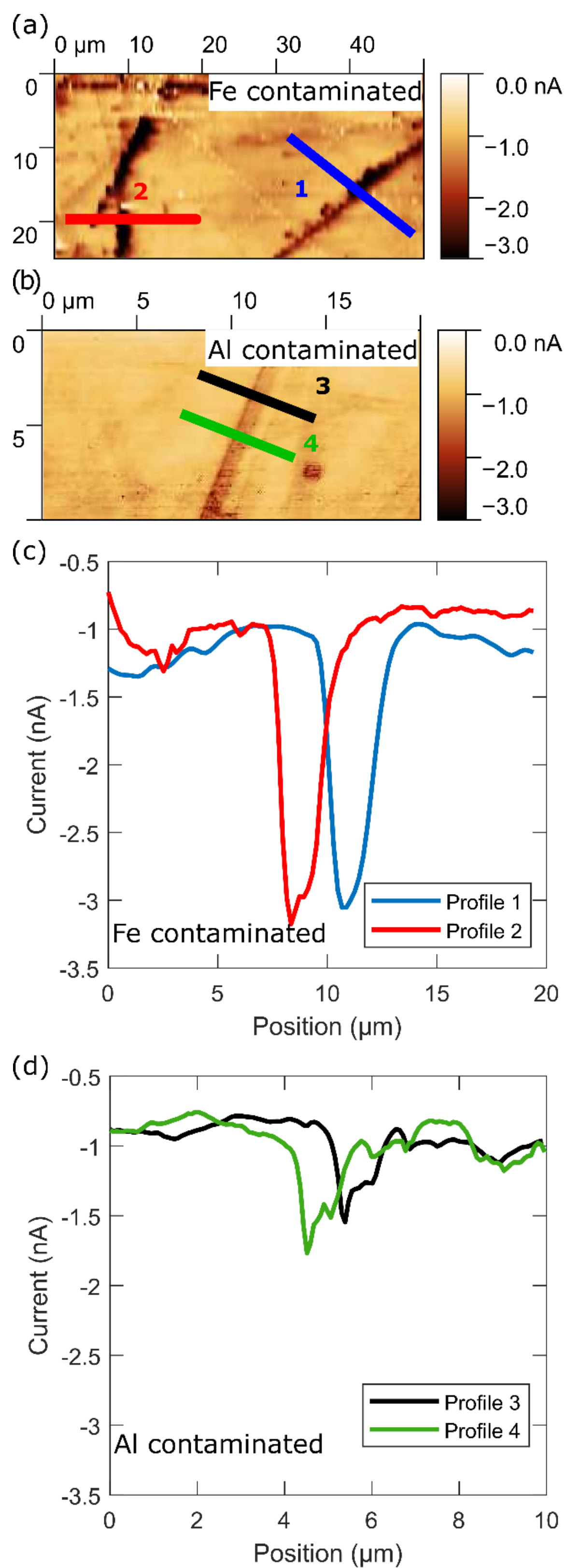

Fig. 3 c-AFM maps of the Fe contaminated and Al contaminated samples (a, b) and the relevant current profiles (c, d) across the line scan sketched in the current maps.

In addition, the GBs of the Fe and Al contaminated samples show different *effective* GB width as estimated by the c-AFM maps. The electrical effect of the GB in Fe contaminated has a spatial extension between 2 and 3 μm [21,27], and the width is not homogeneous, suggesting impurity clustering which can be related to segregation of metallic impurities and/or formation of metallic precipitates at the GB. On the other hand, the GB width in the Al contaminated sample is lower (around 1.5 μm) and more homogeneous. The lateral resolution of the instrument is limited by the size of the tip, and it is generally 100 times larger than atomic scale [28], but, due to the long-range Coulombic interaction, the widths measured in the current maps are still significantly higher than the geometric width of silicon GBs, that usually reaches a few lattice constants [29]. The type of precipitate decorating the GB plays a major role on the electrical properties of the sample: the iron precipitates segregated at the GB of the Fe contaminated sample are likely to be the main cause for the higher current contrast.

Local current-voltage characteristics have been measured by c-AFM on the GB and on the grain in both samples. Measurements were repeated in three different positions on the GBs, and in eight different positions on the grains, and the average curves are shown in Fig. 4. The Pt tip of the c-AFM and the sample can be considered as a Schottky junction, and the resulting current-voltage characteristic is assumed to follow the thermionic emission model. In both cases the tip-sample junctions are forward biased when the sample has a negative applied voltage. The forward current is higher at the GBs, confirming the higher conductivity already observed in the current maps. The GB characteristics in the Al contaminated sample also shows an electrical breakdown voltage at -9 V.

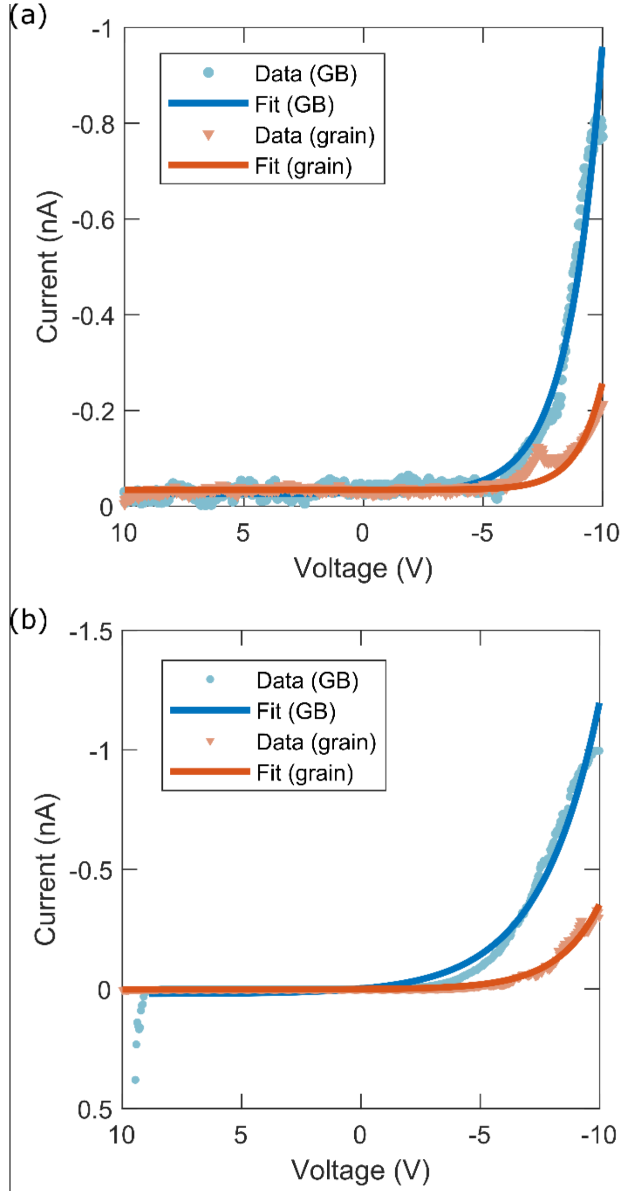

Fig. 4 Current-voltage characteristic of the (a) Fe contaminated and (b) Al contaminated samples on the GB and on the grain.

The characteristics were fitted with the thermionic emission model:

$I = I_s(\mathrm{e}^{-BV} - 1) - I_0 \quad (1)$

Here, I_S is the saturation current $I_s = AA^*T^2\exp[-e\varphi_B/k_BT]$, where A is the area of the Schottky junction, A^* is the Richardson's constant, T is the absolute temperature of the system, e is the elementary charge, φ_B is the Schottky Barrier Height (SBH), and k_B is the Boltzmann constant; the expression for the exponential factor B is e/nk_BT, where n is the ideality factor of the Pt/Si Schottky nano-diode; I_0 is an additional current term related to the surface conduction. The values of I_S, B, and I_0 were extracted from the fit and the SBH was calculated from I_S, using A^*=112 A

cm^{-2} K^{-2}, and T=300 K. The area of the Schottky junction A was estimated as πr_{tip}^2, with the tip radius r_{tip}=20 nm.

The estimated values of φ_B on the grain and on the GB are reported in Table 1, indicating a lowering $\Delta\varphi_B$ of the potential barrier of approximately 0.1 eV at the GB in the Fe contaminated sample and of 0.075 eV in the Al contaminated sample. The values of $\Delta\varphi_B$ could be explained by the presence of different types of precipitates in the two samples.

Sample	**φ_B Grain (eV)**	**φ_B GB (eV)**	**$\Delta\varphi_B$ (eV)**
Fe contaminated	0.5884 ± 0.0005	0.4883 ± 0.0002	0.1
Al contaminated	0.6574 ± 0.0002	0.5818 ± 0.0002	0.075

Table 1 SBH on grain and on GB, estimated from an exponential fit of the curves in Fig. 4.

3.3. Current Profile Modelling

The results reported in Table 1 can be understood on the basis of the hypothesis that FeSi clusters form at the GB. This hypothesis is based on literature comparison: Lal *et al.* [30] report similar values for the SBH (0.59 eV, 0.54 eV, and 0.49 eV) from current-voltage measurements on similar Fe contaminated samples, as-deposited and after annealing at 500 and 600 °C, respectively. The thermal annealing causes an increase in the interface state density, leading to a decrease of φ_B, with the formation of stable β-$FeSi_2$. In another study [31] on a Cz low-doped ([B]=10^{14} cm^{-3}) silicon bi-crystal with a Σ25 GB, the sample face was iron plated, heat treated (1200 °C for 3 hours) and then cooled. This process induced the formation of iron precipitates, giving a SBH of 0.48 eV. Similarly [32], the deposition of iron on *n*- and *p*-type silicon led to the formation of 18 to 35 nm thick layer of β-$FeSi_2$. Current-voltage measurements with silver paste as back contact found that β-$FeSi_2$ is a *p*-type semiconductor with high carrier density (on the order of 10^{18} cm^{-3}).

The presence of β-$FeSi_2$ precipitates might explain the high current contrast between the grain and the GB. Single impurity atoms in a semiconductor introduce band-like states within the bandgap, affecting the carrier lifetime. On the other hand, nucleation and coarsening of metallic precipitates, with a metal-like density of states and their own Fermi level and work function take place. Thus, an internal Schottky junction forms within the Si matrix, with its space charge region around the precipitate that determines the capture rate of the carriers.

The shape of a current profile close to the GB can be modelled by assuming a redistribution of charge density due to a Coulombic potential introduced by a spherical and positively charged (Q) precipitate of radius R_p that is just below the surface (Fig. 5a). The precipitate is set at the origin and R is the distance between the tip and the centre of the precipitate.

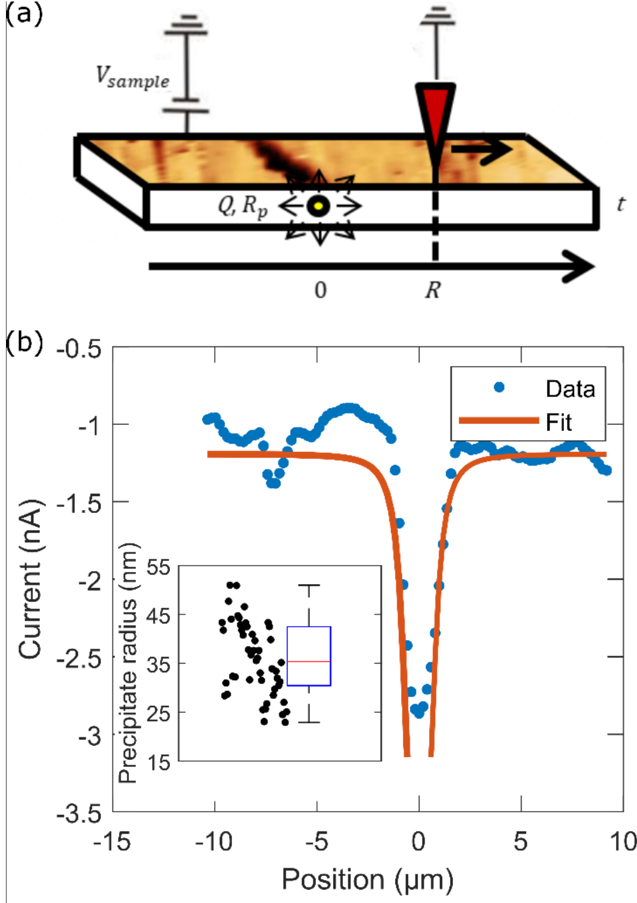

Fig. 5 (a) Schematic of the tip-sample system in a region close to a GB. The charged iron precipitate (yellow) that decorates the GB introduces a Coulombic potential that induces a charge redistribution and changes the current flowing between tip (red) and sample. (b) Experimental current profile across a grain boundary fitted by Equation 3. Inset: distribution of R_p calculated from 50 current profiles.

The hole density profile is affected by the charged precipitate and is assumed to have the shape $p(R) = -c/R^2$. The current density J is given by the usual drift and diffusion terms, but the precipitate introduces an additional electric potential $F(R)$ that modifies the drift term:

$$|J| = -eD_p \frac{\mathrm{d}p}{\mathrm{d}R} + e\mu_p pF(R) + e\mu_p p_0 \frac{V_{sample}}{t} \quad (2)$$

where D_p is the hole diffusion coefficient in silicon, μ_p is the hole mobility, V_{sample} is the applied voltage, t is the thickness of the sample ≈180 μm) and p_0 is the hole density inside the grain. The derivation of the current at the grain boundary is detailed in Appendix A.

Equation 2 can be simplified to:

$$|I| = |J|A = \left(\frac{\alpha}{R^3} + \frac{\beta}{R^4} + \gamma\right)\pi r_{tip}{}^2 \quad (3)$$

and the parameter β is related to Q and R_p:

$$\frac{\beta}{A} = \frac{\mu_p ec}{4\pi\epsilon_s}\left(Q + 4\pi ec R_p\right) \quad (4)$$

Q and R_p are unknowns in the expression of β, and these values are related by the expression of the carrier density ρ_{prec} of a spherical precipitate:

$$\rho_{prec} = \frac{Q/e}{\frac{4}{3}\pi R_p{}^3} \quad (5)$$

The reported values for ρ_{prec} are between 10^{18} and 10^{20} cm^{-3} [33]. For these calculations ρ_{prec} = 3 × 10^{19} cm^{-3} was assumed [33]. Fig. 5b shows the fit on the current profile using Equation 3 and R_p was estimated with Equations 4 and 5. This fit was repeated for 50 consecutive current profiles in the c-AFM scan to improve the statistics on the estimation of the parameters and a distribution with an average precipitate radius of R_p = (36 ± 7) nm was obtained (the distribution of R_p is shown in the inset of Fig. 5b).

With ρ_{prec} fixed at 10^{18} cm^{-3} and 10^{20} cm^{-3}, the average R_p becomes (110 ± 20) nm and (24 ± 5) nm, respectively, in agreement with literature values [33–35].

4. Conclusions

In this study, wafers from two mc-Si ingots were investigated in order to characterize the electrical activity of iron and aluminium decorated GBs, as these defects severely affect the performance of silicon-based photovoltaic devices. The total GB density and the density of $\Sigma 3^n$ GBs, measured by means of EBSD, decrease from the bottom to the top of both ingots. These structural defects affect the electrical properties of the material as they are a source of dislocations, but most importantly are segregation sites for electrically active metallic precipitates. A nano-scale electrical characterization performed with c-AFM allowed to identify, with submicron resolution, regions of GBs that are strongly active as recombination sites. Thus, it was possible to study how metallic precipitates locally affect the electrical properties of mc-Si wafers. The increased current flow observed at the GBs can be explained by the presence of metal-silicide phases and the effect on the electrical properties of the sample depends on the type of contaminant. Iron-related precipitates are more recombination active compared to aluminium ones and their electrical effect is spatially inhomogeneous along a GB. The hypothesis of metallic precipitation was corroborated by local current-voltage characteristics measured on the GB and on the neighbouring grains, that were modelled assuming thermionic emission as the principal mechanism of electrical conduction.

The Schottky Barrier Height decreases at the GB with respect to the grain, due to the formation of metallic precipitates that introduce a metal-like density of states at the GBs. From the current profiles measured across GBs by c-AFM, it was possible to estimate a precipitate radius of few tens of nm, by assuming that it introduces the Coulombic potential of a positively charged sphere, therefore modifying locally the conductivity of the sample. This shows that c-AFM analyses and modelling are powerful tools for the understanding of electrical activity of metallic precipitates in mc-Si.

Acknowledgements

The authors would like to acknowledge Tobias Cramer at UniBo for training and assistance on c-AFM measurements, Gaute Stokkan and Birgit Ryningen at SINTEF Industry (Norway) for their insightful suggestions. Part of this work was supported by the KPN-CruGenSi (Crucibles for next generation high quality silicon solar cells) contract nr. 268027.

Data availability

The data that support the findings of this study are available from the corresponding author upon reasonable request.

Appendix

A. Current profile derivation

The shape of a current profile close to the GB can be modelled by assuming a redistribution of charge density due to a Coulombic potential introduced by a spherical and positively charged (Q) precipitate of radius R_p that is just below the surface. The precipitate is set at the origin and R is the distance between the tip and the center of the precipitate. The hole density profile is affected by the charged precipitate and is assumed to have the shape $p(R) = -c/R^2$. The current density J is given by the usual drift and diffusion terms, but the precipitate introduces an additional electric potential $F(R)$ that modifies the drift term:

$$|J| = -eD_p \frac{\mathrm{d}p}{\mathrm{d}R} + e\mu_p pF(R) + e\mu_p p_0 \frac{V_{sample}}{t} \text{ (A1)}$$

where D_p is the hole diffusion coefficient in silicon, μ_p is the hole mobility, V_{sample} is the applied voltage, t is the thickness of the sample ≈180 μm) and p_0 is the hole density inside the grain. The Coulombic potential is given by the charge Q of the precipitate and by the carrier density integrated for $R>R_p$:

$F(R) = \frac{1}{4\pi\epsilon_s R^2}\left[Q + 4\pi e \int_{R_p}^{R} (p - n - N_a) r^2 dr\right]$ (A2)

but, as the sample is p-type, it is possible to approximate $p - n - N_a \approx p$, so Equation A2 becomes:

$$F(R) = \frac{1}{4\pi\epsilon_s R^2}\left[Q + 4\pi e \int_{R_p}^{R} p(r) r^2 dr\right] = \frac{1}{4\pi\epsilon_s R^2}\left[Q - 4\pi e \int_{R_p}^{R} c dr\right]$$

$= \frac{1}{4\pi\epsilon_s R^2}\left[Q - 4\pi e c\left(R - R_p\right)\right]$ (A3)

Combining Equations A1 and A3, the expression for the absolute value of the current density as a function of the distance R from the precipitate becomes:

$|J| = \frac{1}{R^3}\left(-2D_p e c + \frac{\mu_p e^2 c^2}{\epsilon_s}\right) - \frac{1}{R^4}\frac{\mu_p e c}{4\pi\epsilon_s}\left(Q + 4\pi e c R_p\right) + e\mu_p p_0 \frac{V_{sample}}{t}$ (A4)

which can be related to the current and simplified to:

$|I| = |J|A = \left(\frac{\alpha}{R^3} + \frac{\beta}{R^4} + \gamma\right)\pi {r_{tip}}^2$ (A5)

where the expression for the parameters α, β, and γ can be extracted from Equation A4:

$\alpha = -2D_p e c + \frac{\mu_p e^2 c^2}{\epsilon_s}$ (A6a)

$\beta = \frac{\mu_p e c}{4\pi\epsilon_s}\left(Q + 4\pi e c R_p\right)$ (A6b)

$\gamma = e\mu_p p_0 \frac{V_{sample}}{t}$ (A6c)

References

[1] C. Donolato, Modeling the effect of dislocations on the minority carrier diffusion length of a semiconductor, J. Appl. Phys. 84 (1998) 2656–2664. https://doi.org/10.1063/1.368378.

[2] J. Chen, T. Sekiguchi, Carrier Recombination Activity and Structural Properties of Small-Angle Grain Boundaries in Multicrystalline Silicon, Jpn. J. Appl. Phys. 46 (2007) 6489–6497. https://doi.org/10.1143/JJAP.46.6489.

[3] J. Chen, T. Sekiguchi, D. Yang, F. Yin, K. Kido, S. Tsurekawa, Electron-beam-induced current study of grain boundaries in multicrystalline silicon, J. Appl. Phys. 96 (2004) 5490–5495. https://doi.org/10.1063/1.1797548.

[4] T. Buonassisi, A.A. Istratov, M.D. Pickett, M. Heuer, J.P. Kalejs, G. Hahn, M.A. Marcus, B. Lai, Z. Cai, S.M. Heald, T.F. Ciszek, R.F. Clark, D.W. Cunningham, A.M. Gabor, R.

Jonczyk, S. Narayanan, E. Sauar, E.R. Weber, Chemical natures and distributions of metal impurities in multicrystalline silicon materials, Prog. Photovoltaics Res. Appl. 14 (2006) 513–531. https://doi.org/https://doi.org/10.1002/pip.690.

[5] E. Olsen, E.J. Øvrelid, Silicon nitride coating and crucible—effects of using upgraded materials in the casting of multicrystalline silicon ingots, Prog. Photovoltaics Res. Appl. 16 (2008) 93–100. https://doi.org/https://doi.org/10.1002/pip.777.

[6] J. Hofstetter, J.F. Lelièvre, D.P. Fenning, M.I. Bertoni, T. Buonassisi, C. del Cañizo, Towards the Tailoring of P Diffusion Gettering to As-Grown Silicon Material Properties, Solid State Phenom. 178–179 (2011) 158–165. https://doi.org/10.4028/www.scientific.net/SSP.178-179.158.

[7] S. Rein, S.W. Glunz, Electronic properties of interstitial iron and iron-boron pairs determined by means of advanced lifetime spectroscopy, J. Appl. Phys. 98 (2005) 113711. https://doi.org/10.1063/1.2106017.

[8] J.R. Davis, A. Rohatgi, R.H. Hopkins, P.D. Blais, P. Rai-Choudhury, J.R. McCormick, H.C. Mollenkopf, Impurities in silicon solar cells, IEEE Trans. Electron Devices. 27 (1980) 677–687. https://doi.org/10.1109/T-ED.1980.19922.

[9] G. Coletti, P.C.P. Bronsveld, G. Hahn, W. Warta, D. Macdonald, B. Ceccaroli, K. Wambach, N. Le Quang, J.M. Fernandez, Impact of Metal Contamination in Silicon Solar Cells, Adv. Funct. Mater. 21 (2011) 879–890. https://doi.org/https://doi.org/10.1002/adfm.201000849.

[10] A.A. Istratov, T. Buonassisi, R.J. McDonald, A.R. Smith, R. Schindler, J.A. Rand, J.P. Kalejs, E.R. Weber, Metal content of multicrystalline silicon for solar cells and its impact on minority carrier diffusion length, J. Appl. Phys. 94 (2003) 6552–6559. https://doi.org/10.1063/1.1618912.

[11] W.S. I.E. Reis, S. Riepe, W. Koch, J. Bauer, S. Beljakowa, O. Breitenstein, H. Habenicht, D. Kreßner-Kiel, G. Pensl, J. Schön, Effect of Impurities on Solar Cell Parameters in Intentionally Contaminated Multicrystalline Silicon, in: 24th Eur. Photovolt. Sol. Energy Conf., Hamburg, 2009: pp. 2144–2148.

[12] J. Tan, D. Macdonald, N. Bennett, D. Kong, A. Cuevas, I. Romijn, Dissolution of metal precipitates in multicrystalline silicon during annealing and the protective effect of phosphorus emitters, Appl. Phys. Lett. 91 (2007) 043505. https://doi.org/10.1063/1.2766664.

[13] R. Krain, S. Herlufsen, J. Schmidt, Internal gettering of iron in multicrystalline silicon at low temperature, Appl. Phys. Lett. 93 (2008) 152108. https://doi.org/10.1063/1.2987521.

[14] R.C. Newman, Defects in silicon, Reports Prog. Phys. 45 (1982) 1163–1210. https://doi.org/10.1088/0034-4885/45/10/003.

[15] O.K. von Goldbeck, Fe—Si Iron—Silicon BT - IRON—Binary Phase Diagrams, in: O.K. von Goldbeck (Ed.), Springer Berlin Heidelberg, Berlin, Heidelberg, 1982: pp. 136–139. https://doi.org/10.1007/978-3-662-08024-5_62.

[16] N. Onda, J. Henz, E. Müller, K.A. Mäder, H. von Känel, Epitaxy of fluorite-structure silicides: metastable cubic FeSi2 on Si(111), Appl. Surf. Sci. 56–58 (1992) 421–426. https://doi.org/https://doi.org/10.1016/0169-4332(92)90264-X.

[17] D. Leong, M. Harry, K.J. Reeson, K.P. Homewood, A silicon/iron-disllicide light-emitting diode operating at a wavelength of 1.5 μm, Nature. 387 (1997) 686–688. https://doi.org/10.1038/42667.

[18] D. Cavalcoli, F. Detto, M. Rossi, A. Tomasi, A. Cavallini, The electrical conductivity of hydrogenated nanocrystalline silicon investigated at the nanoscale, Nanotechnology. 21 (2010) 045702. https://doi.org/10.1088/0957-4484/21/4/045702.

[19] B. Rezek, J. Stuchlík, A. Fejfar, J. Kočka, Microcrystalline silicon thin films studied by atomic force microscopy with electrical current detection, J. Appl. Phys. 92 (2002) 587–593. https://doi.org/10.1063/1.1486032.

[20] D. Azulay, I. Balberg, V. Chu, J.P. Conde, O. Millo, Current routes in hydrogenated microcrystalline silicon, Phys. Rev. B. 71 (2005) 113304. https://doi.org/10.1103/PhysRevB.71.113304.

[21] M. Rumler, M. Rommel, J. Erlekampf, M. Azizi, T. Geiger, A.J. Bauer, E. Meißner, L. Frey, Characterization of grain boundaries in multicrystalline silicon with high lateral resolution using conductive atomic force microscopy, J. Appl. Phys. 112 (2012) 034909. https://doi.org/10.1063/1.4746742.

[22] D. Cavalcoli, M. Rossi, A. Tomasi, A. Cavallini, Degeneracy and instability of nanocontacts between conductive tips and hydrogenated nanocrystalline Si surfaces in conductive atomic force microscopy, Nanotechnology. 20 (2009) 045702. https://doi.org/10.1088/0957-4484/20/4/045702.

[23] G. Stokkan, A. Song, B. Ryningen, Investigation of the Grain Boundary Character and Dislocation Density of Different Types of High Performance Multicrystalline Silicon, Crystals. 8 (2018) 341. https://doi.org/10.3390/cryst8090341.

[24] T. Ervik, M. Kivambe, G. Stokkan, B. Ryningen, O. Lohne, Dislocation Formation at Sigma =27a Boundaries in Multicrystalline Silicon for Solar Cells, in: 26th Eur. Photovolt. Sol. Energy Conf., WIP-Renewables;, Munich, 2011: pp. 1895–1899. https://www.tib.eu/de/suchen/id/BLCP%3ACN081120259.

[25] K. Adamczyk, R. Søndenå, G. Stokkan, E. Looney, M. Jensen, B. Lai, M. Rinio, M. Di

Sabatino, Recombination activity of grain boundaries in high-performance multicrystalline Si during solar cell processing, J. Appl. Phys. 123 (2018) 055705. https://doi.org/10.1063/1.5018797.

[26] K. Adamczyk, R. Søndenå, C.C. You, G. Stokkan, J. Lindroos, M. Rinio, M. Di Sabatino, Recombination Strength of Dislocations in High-Performance Multicrystalline/Quasi-Mono Hybrid Wafers During Solar Cell Processing, Phys. Status Solidi. 215 (2018) 1700493. https://doi.org/https://doi.org/10.1002/pssa.201700493.

[27] J. Oualid, C.M. Singal, J. Dugas, J.P. Crest, H. Amzil, Influence of illumination on the grain boundary recombination velocity in silicon, J. Appl. Phys. 55 (1984) 1195–1205. https://doi.org/10.1063/1.333161.

[28] S.S. Hong, J.J. Cha, Y. Cui, One Nanometer Resolution Electrical Probe via Atomic Metal Filament Formation, Nano Lett. 11 (2011) 231–235. https://doi.org/10.1021/nl103603v.

[29] C.R.M. Grovenor, Grain boundaries in semiconductors, J. Phys. C Solid State Phys. 18 (1985) 4079–4119. https://doi.org/10.1088/0022-3719/18/21/008.

[30] C. Lal, R. Dhunna, I.P. Jain, Structural, magnetic and electrical properties of Fe/Si system, Mater. Sci. Semicond. Process. 11 (2008) 1–5. https://doi.org/https://doi.org/10.1016/j.mssp.2008.04.004.

[31] A. Ihlal, R. Rizk, Effects of iron contamination on the electrical activity of a silicon bicrystal, J. Phys. D. Appl. Phys. 29 (1996) 3096–3100. https://doi.org/10.1088/0022-3727/29/12/023.

[32] K. Lefki, P. Muret, N. Cherief, R.C. Cinti, Optical and electrical characterization of β-$FeSi_2$ epitaxial thin films on silicon substrates, J. Appl. Phys. 69 (1991) 352–357. https://doi.org/10.1063/1.347720.

[33] M. Suzuno, Y. Ugajin, S. Murase, T. Suemasu, M. Uchikoshi, M. Isshiki, Effect of using a high-purity Fe source on the transport properties of p-type β-FeSi2 grown by molecular-beam epitaxy, J. Appl. Phys. 102 (2007) 103706. https://doi.org/10.1063/1.2816230.

[34] D.P. Fenning, J. Hofstetter, M.I. Bertoni, S. Hudelson, M. Rinio, J.F. Lelièvre, B. Lai, C. del Cañizo, T. Buonassisi, Iron distribution in silicon after solar cell processing: Synchrotron analysis and predictive modeling, Appl. Phys. Lett. 98 (2011) 162103. https://doi.org/10.1063/1.3575583.

[35] D.P. Fenning, J. Hofstetter, M.I. Bertoni, G. Coletti, B. Lai, C. del Cañizo, T. Buonassisi, Precipitated iron: A limit on gettering efficacy in multicrystalline silicon, J. Appl. Phys. 113 (2013) 044521. https://doi.org/10.1063/1.4788800.

Iron related precipitates in multicrystalline silicon by Conductive Atomic Force Microscopy

Pierpaolo Vecchi,[1, a)] Giovanni Armaroli,[1] Marisa Di Sabatino,[2] and Daniela Cavalcoli[1]

[1)] *Department of Physics and Astronomy, University of Bologna, Viale Berti Pichat 6/2, 40127 Bologna, Italy*

[2)] *Department of Materials Science and Engineering, NTNU, A. Getz vei 2B, NO-7491 Trondheim, Norway*

[a)] *Corresponding author's email address:* pierpaolo.vecchi2@unibo.it

<u>Topography maps</u>

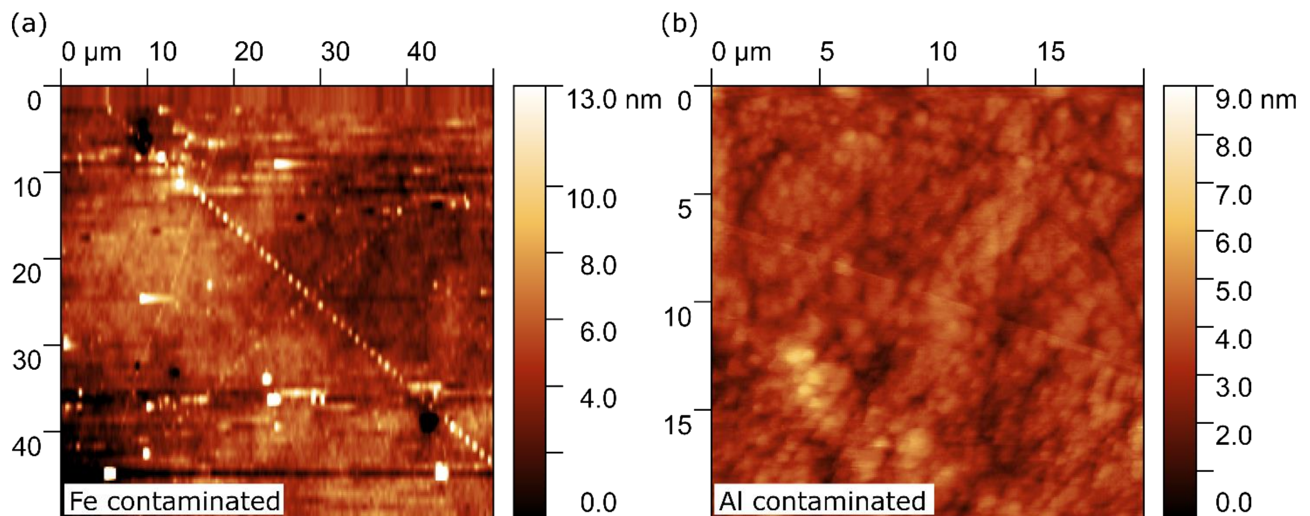

Fig. A.1 Topography maps of (a) Fe contaminated and (b) Al contaminated samples.